GEOPHYSICS, VOL. 71, NO. 5 (SEPTEMBER-OCTOBER 2006); P. S169–S177, 10 FIGS., 1 TABLE.
10.1190/1.2227619

Wave-equation-based seismic illumination analysis

Xiao-Bi Xie[1], Shengwen Jin[2], and Ru-Shan Wu[1]

ABSTRACT

We present a wave-equation-based method for seismic illumination analysis. A one-way wave-equation-based, generalized screen propagator is used to extrapolate the wavefields from sources and receivers to the subsurface target. A local plane-wave analysis is used at the target to calculate localized, directional energy fluxes for both source and receiver wavefields. We construct an illumination matrix using these energy fluxes to quantify the target illumination conditions. The target geometry information is used to manipulate the illumination matrix and generate different types of illumination measures. The wave-equation-based approach can properly handle forward multiple-scattering phenomena, including focusing/defocusing, diffraction, and interference effects. It can be directly applied to complex velocity models. Velocity-model smoothing and Fresnel-zone smoothing are not required. Different illumination measurements derived from this method can be applied to target-oriented or volumetric illumination analyses. This new method is flexible and practical for illumination analysis in complex 2D and 3D velocity models with nontrivial acquisition and target geometries.

INTRODUCTION

The illumination of a subsurface target is affected by many factors, e.g., the limited acquisition geometry, the complex overburden structure, and the reflector dip angle. An uneven illumination causes a distorted image. Seismic illumination analysis quantifies such image distortion and has many applications in seismic migration/imaging. The effect of acquisition geometry can be evaluated by calculating illuminations of different shooting patterns. More accurate amplitude variation with angle (AVA) or amplitude variation with offset (AVO) may be obtained if the observation is corrected with angle-dependent illumination.

In the past, the illumination estimate was based simply on the acquisition geometry at the surface under the assumption of a homogeneous velocity model, horizontal targets, and symmetric raypaths (Hoffmann, 2001). These assumptions may be invalid for complex structures under realistic situations. To properly calculate the target illumination, we have to extrapolate the wavefield between sources, targets, and receivers. In order to calculate the angle-dependent illumination, we also need directional information from the wavefield.

Traditionally, illumination and resolution analyses have used the ray-based method (Schneider and Winbow, 1999; Bear et al., 2000). The ray-based method can provide both intensity and directional information carried in the wavefield. Dynamic ray tracing is used to calculate energy propagation along the source-target-receiver path using the smoothed velocity model. The common reflection point (CRP) gathers (ray amplitude, hit count, offset coverage, etc.) on the target are used for the illumination measurements. A Fresnel-zone smoothing is usually applied to obtain smoothly distributed coverage on the target horizon (Muerdter and Ratcliff, 2001a, b). These procedures have been discussed by Muerdter and Ratcliff (2001a, b) and Muerdter et al. (2001), who made a comprehensive demonstration of the application of ray-based illumination analysis in the subsalt region. Using common focusing point (CFP) analysis, Berkhout et al. (2001) and Volker et al. (2001) investigated the effect of acquisition geometry on target illumination and migration resolution. Hoffmann (2001) used the illumination information for resolution analysis. Based on the illumination analysis in the local-angle domain, Gelius et al. (2002) and Lecomte et al. (2003) defined a resolution function and discussed the effect of a complex velocity model on the illumination and resolution.

Although the ray-based illumination analysis can handle both irregular acquisition geometry and laterally varying velocity models, the high-frequency asymptotic approximation and the caustics inherent in ray theory may severely limit its accuracy in complex regions (Hoffmann, 2001). While the ray-based method is relatively efficient for target-oriented analysis, it is still not a cost-effective approach for full-volume 3D illumination analysis. Attempts have been made to apply the wave-equation-based method to seismic illumination and resolution analysis. Schuster and Hu (2000) derived an

Presented at the 74th Annual Meeting, Society of Exploration Geophysicists, October 2004. Manuscript received by the Editor March 3, 2005; revised manuscript received January 24, 2006; published online August 28, 2006.
[1]IGPP/CSIDE, University of California at Santa Cruz, 1156 High Street, Santa Cruz, California 95064. E-mail: xie@pmc.ucsc.edu; wrs@pmc.ucsc.edu.
[2]Screen Imaging Technology, Incorporated, 1322 Southwest Freeway, Suite 1508, Houston, Texas 77074. E-mail: jin@screenimaging.com.

analytical solution for target point-scatter responses by assuming a homogeneous velocity model with continuously distributed sources and receivers. Rickett (2003) developed a normalization scheme to compensate for the effect of irregular illumination. However, these results were usually restricted to simple geometries or did not provide directional information that is crucial for target-oriented illumination.

Recently developed dual-domain, one-way wave-equation-based methods (e.g., Stoffa et al., 1990; Ristow and Ruhl, 1994; Xie and Wu, 1998, 2005; Jin et al., 1998, 2002; Huang et al., 1999; Xie et al., 2000; Wu and Chen, 2001; and Biondi, 2002) provide propagators for seismic-wave extrapolation in complex velocity models. Although these propagators neglect reverberations between heterogeneous layers, they properly handle forward multiple-scattering phenomena, including focusing/defocusing, diffraction, and wave-interference effects. These algorithms alternate between the space domain and wavenumber domain using the fast Fourier transform (FFT). These methods make optimal operations in each domain, resulting in a fast and accurate extrapolation of the wavefield. This makes them suitable for seismic forward modeling and migration/imaging. However, the inability to provide localized-angle information prevents them from being used for directional illumination calculations.

There have been attempts to calculate angle information using the wave-equation-based methods. The offset plane wave and related offset angle generated from offset-domain migration have been used in the velocity updating (Prucha et al., 1999; Mosher et al., 2001). Such angle information does not directly relate to the wave-propagation direction and cannot be used in illumination analysis. To extract angle information from the wavefield, Xie and Wu (2002) proposed an approach based on a local plane-wave analysis. Through local slant stacking or a windowed Fourier transform, the approach provides localized-angle information. Xie et al. (2003) tested the local plane-wave analysis method in illumination analysis. Wu and Chen (2002, 2003) and Wu et al. (2003) used wavelet-transform theory (Gabor-Daubechie frame) to decompose the wavefield into components with localized angles for illumination analysis. Jin and Walraven (2003) applied the directional illumination to investigate the causes of subsalt-imaging shadows.

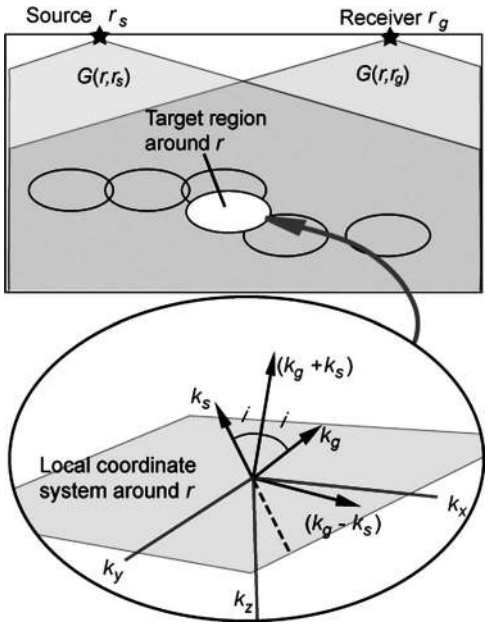

Figure 1. Diagram of the coordinate system.

In this research, we present an illumination-analysis method using the generalized screen propagator (Xie and Wu, 1998) and the local plane-wave analysis (Xie and Wu, 2002; Xie et al., 2003). The wave-equation-based propagator extrapolates the wavefields from sources and receivers to the target region. Local plane-wave analysis is conducted at the target position to obtain localized, directional energy fluxes for both source and receiver wavefields. From these energy fluxes, we construct a local illumination matrix to describe the target illumination. By manipulating the illumination matrix, different illumination measures can be calculated. We use several 2D and 3D numerical examples to demonstrate the potential applications of these illumination measurements.

METHODS

Consider using a survey system composed of a source located at $\mathbf{r}_s$ and a receiver located at $\mathbf{r}_g$ to investigate a small, subsurface target region $V(\mathbf{r})$ in the vicinity of location $\mathbf{r}$ (see Figure 1). The source sends a seismic wave to the target. Within the target region, the incident wave interacts with the reflector and generates a reflected or scattered wave that propagates from the target to the receiver. Using the multiple forward-scattering/single-backscattering approximation, the seismic wave at the receiver can be expressed as

$$u(\mathbf{r},\mathbf{r}_s,\mathbf{r}_g) = 2k_0^2 \int_V m(\mathbf{r}')G(\mathbf{r}';\mathbf{r}_s)G(\mathbf{r}';\mathbf{r}_g)dv', \quad (1)$$

where $\mathbf{r}'$ is a local coordinate within $V(\mathbf{r})$, $m(\mathbf{r}') = \delta c/c(\mathbf{r}')$ is the velocity perturbation, $c(\mathbf{r}')$ is the velocity, $k_0 = \omega/c_0(\mathbf{r})$ is the background wavenumber, $c_0(\mathbf{r})$ is the local background velocity inside $V(\mathbf{r})$, ω is the angular frequency, and $G(\mathbf{r}';\mathbf{r}_s)$ and $G(\mathbf{r}';\mathbf{r}_g)$ are Green's functions with sources at $\mathbf{r}_s$ and $\mathbf{r}_g$, respectively. The reciprocity theorem $G(\mathbf{r}';\mathbf{r}_g) = G(\mathbf{r}_g;\mathbf{r}')$ has been used. For simplicity, the apparent frequency dependence has been omitted from equation 1 and all the following equations. Considering that V is small and the Green's functions mostly propagate in the background-velocity medium, we choose to use one-way wave-equation-based propagators (Xie and Wu, 1998) to calculate these Green's functions.

Applying the local plane-wave decomposition (Xie and Wu, 2002; Xie et al., 2003) within V, the Green's functions are decomposed as

$$G(\mathbf{r}';\mathbf{r}_s) = \int G(\mathbf{K},\mathbf{r};\mathbf{r}_s)e^{i\mathbf{k}\cdot\mathbf{r}'}d\mathbf{K},$$

$$G(\mathbf{r}';\mathbf{r}_g) = \int G(\mathbf{K},\mathbf{r};\mathbf{r}_g)e^{i\mathbf{k}\cdot\mathbf{r}'}d\mathbf{K}. \quad (2)$$

By substituting equation 2 into equation 1, we have

$$u(\mathbf{r},\mathbf{r}_s,\mathbf{r}_g) = 2k_0^2 \iint G(\mathbf{K}_s,\mathbf{r};\mathbf{r}_s)G(\mathbf{K}_g,\mathbf{r};\mathbf{r}_g) \times m(\mathbf{r},\mathbf{k}_g + \mathbf{k}_s)d\mathbf{K}_g d\mathbf{K}_s, \quad (3)$$

where

$$m(\mathbf{r},\mathbf{k}_g+\mathbf{k}_s)=\int_V m(\mathbf{r}')e^{i(\mathbf{k}_g+\mathbf{k}_s)\cdot\mathbf{r}'}dv'. \quad (4)$$

In equations 2–4, $\mathbf{k}=\mathbf{K}+k_z\hat{\mathbf{e}}_z$ is the local wavenumber, $\mathbf{K}$ is the horizontal wavenumber, k_z is the vertical wavenumber, $\hat{\mathbf{e}}_z$ is the vertical unit vector, $\mathbf{k}_s=\mathbf{K}_s+k_{sz}\hat{\mathbf{e}}_z$, and $\mathbf{k}_g=\mathbf{K}_g+k_{gz}\hat{\mathbf{e}}_z$ are local transforms with respect to $\mathbf{r}'$ (not $\mathbf{r}_s$ and $\mathbf{r}_g$), and k_{sz} and k_{gz} are vertical components of $\mathbf{k}_s$ and $\mathbf{k}_g$, respectively. Subscripts s and g denote the source-side and receiver-side wavefields, respectively. Given the local reference velocity $c_0(\mathbf{r})$, the components of the wavenumber are not fully independent, i.e., $k_x^2+k_y^2+k_z^2=k_0^2$, and k_z can be determined from its horizontal component via $k_z=\sqrt{k_0^2-K^2}$. We retain the parameter $\mathbf{r}$ in these equations to indicate the location of the target region. Equation 3 links the observation with the source and subsurface target and forms the basis of many seismic methods (e.g., seismic modeling, migration, inversion, and tomography). Taking equation 3 as the starting point, we adopt the mean square of the Green's function to define the illumination. Usually, a fictitious plane reflector with a dipping angle and a unit (or constant) reflectivity is required for calculating the illumination (Muerdter and Ratcliff, 2001a). To generalize this into an arbitrarily nonflat reflector, we substitute $m(\mathbf{r},\mathbf{k}_g+\mathbf{k}_s)$, which can be regarded as a wavenumber-domain local reflectivity, with its normalized amplitude spectrum. A target illumination-response function is then defined as

$$D(\mathbf{r},\mathbf{r}_s,\mathbf{r}_g)=\iint A(\mathbf{r},\mathbf{K}_s,\mathbf{K}_g;\mathbf{r}_s,\mathbf{r}_g)M(\mathbf{r},\mathbf{k}_g+\mathbf{k}_s)d\mathbf{K}_g d\mathbf{K}_s, \quad (5)$$

where $M(\mathbf{r},\mathbf{k})=|m(\mathbf{r},\mathbf{k})|$, and

$$A(\mathbf{r},\mathbf{K}_s,\mathbf{K}_g;\mathbf{r}_s,\mathbf{r}_g)=2k_0^2I(\mathbf{K}_s,\mathbf{r};\mathbf{r}_s)I(\mathbf{K}_g,\mathbf{r};\mathbf{r}_g) \quad (6)$$

is the local illumination matrix of the source-receiver pair $(\mathbf{r}_s,\mathbf{r}_g)$. The equations

$$I(\mathbf{K}_s,\mathbf{r};\mathbf{r}_s)=G(\mathbf{K}_s,\mathbf{r};\mathbf{r}_s)G^*(\mathbf{K}_s,\mathbf{r};\mathbf{r}_s) \quad (7)$$

and

$$I(\mathbf{K}_g,\mathbf{r};\mathbf{r}_g)=G(\mathbf{K}_g,\mathbf{r};\mathbf{r}_g)G^*(\mathbf{K}_g,\mathbf{r};\mathbf{r}_g) \quad (8)$$

are mean squares of the Green's functions, which are proportional to energy fluxes from the source and receiver to the target, respectively. The superscript * denotes complex conjugation.

For a system composed of multiple sources and receivers, the illumination response can be calculated by stacking contributions from individual source-receiver pairs. From equation 5,

$$D(\mathbf{r})=\sum_{\mathbf{r}_s}\sum_{\mathbf{r}_g}D(\mathbf{r},\mathbf{r}_s,\mathbf{r}_g)=\iint A(\mathbf{r},\mathbf{K}_s,\mathbf{K}_g)\times M(\mathbf{r},\mathbf{k}_g+\mathbf{k}_s)d\mathbf{K}_s d\mathbf{K}_g, \quad (9)$$

where

$$A(\mathbf{r},\mathbf{K}_s,\mathbf{K}_g)=\sum_{\mathbf{r}_s}\sum_{\mathbf{r}_g}A(\mathbf{r},\mathbf{K}_s,\mathbf{K}_g;\mathbf{r}_s,\mathbf{r}_g) \quad (10)$$

is the local illumination matrix for the entire acquisition system. The summations over $\mathbf{r}_s$ and $\mathbf{r}_g$ are based on the acquisition geometry. In equation 9, for a given acquisition geometry and background velocity model, the matrix $A(\mathbf{r},\mathbf{K}_s,\mathbf{K}_g)$ is composed of all possible local scattering events $(\mathbf{k}_s,\mathbf{k}_g)$ that may contribute to the target illumination. For a particular local-target structure, $M(\mathbf{r},\mathbf{k})$ provides the mapping relationship between the incident and scattered waves and manipulates energy within the local illumination matrix. The integral sums the energy that can actually contribute to the particular target and gives the illumination response at location $\mathbf{r}$. The effects of acquisition configuration, the background velocity model, and target geometry are all included in the calculation. The illumination response function is calculated using the mean square of the amplitude. When the amplitude is preferred, the root mean square (rms) of $D(\mathbf{r})$ can be used.

For a 3D velocity model, equations 9 and 10 are defined in the acquisition-wavenumber space $(\mathbf{k}_s,\mathbf{k}_g)$, resulting in a 4D illumination matrix. The illumination matrix can be defined in the target-spectrum space through the transformations (see Figure 1)

$$\begin{aligned}\mathbf{k}_d&=\mathbf{k}_g+\mathbf{k}_s,\\ \mathbf{k}_r&=\mathbf{k}_g-\mathbf{k}_s,\end{aligned} \quad (11)$$

or

$$\begin{aligned}\mathbf{K}_d&=\mathbf{K}_g+\mathbf{K}_s,\\ \mathbf{K}_r&=\mathbf{K}_g-\mathbf{K}_s.\end{aligned} \quad (12)$$

Note that after the transformations, the lengths of vectors $\mathbf{k}_d$ and $\mathbf{k}_r$ are no longer of constant value k_0. To determine their vertical components, we have to go back to $\mathbf{k}_s$ and $\mathbf{k}_g$. The illumination matrix can also be defined using two sets of directions (angles) $(\boldsymbol{\theta}_s,\boldsymbol{\theta}_g)$, where $\boldsymbol{\theta}_s=(\theta_s,\varphi_s)$ and $\boldsymbol{\theta}_g=(\theta_g,\varphi_g)$ are incidence and scattering directions, and θ and φ are the corresponding dip and azimuth angles. The relationship between the wavenumber and angles is $\mathbf{k}=k_0(\sin\theta\cos\varphi\hat{\mathbf{e}}_x+\sin\theta\sin\varphi\hat{\mathbf{e}}_y+\cos\theta\hat{\mathbf{e}}_z)$. Therefore, equation 9 can be expressed using either $(\mathbf{K}_s,\mathbf{K}_g)$, $(\mathbf{K}_d,\mathbf{K}_r)$, or $(\boldsymbol{\theta}_s,\boldsymbol{\theta}_g)$ with proper Jacobians included.

For a locally planar, dipping structure (i.e., the Kirchhoff scattering model) given by $m(\mathbf{r}')\sim\delta(\mathbf{r}'\cdot\mathbf{n})$, we have $M(\mathbf{k})\sim\delta(\mathbf{k}-C\mathbf{n})$ and $\mathbf{k}_g+\mathbf{k}_s=C\mathbf{n}$, where $\mathbf{n}$ is the normal vector of the reflector, and δ is Dirac's delta function. Since $|\mathbf{k}_s|=|\mathbf{k}_g|=k_0$, we know $\mathbf{n}$ is the angle bisector of $\mathbf{k}_g$ and $\mathbf{k}_s$ (see Figure 1), and $C=2\mathbf{k}_g\cdot\mathbf{n}=2\mathbf{k}_s\cdot\mathbf{n}=2k_0\cos i$ with i as the reflection angle. Substituting this $M(\mathbf{k})$ into equation 9 yields

$$\begin{aligned}D(\mathbf{r},\mathbf{n})&=\iint A(\mathbf{r},\mathbf{K}_s,\mathbf{K}_g)\delta(\mathbf{K}_g+\mathbf{K}_s-C\mathbf{N})d\mathbf{K}_s d\mathbf{K}_g\\ &=\int A(\mathbf{r},C\mathbf{N}-\mathbf{K}_g,\mathbf{K}_g)d\mathbf{K}_g,\end{aligned} \quad (13)$$

where $\mathbf{N}$ is the horizontal component of normal vector $\mathbf{n}$. Since $\mathbf{n}$ is a unit vector, it is determined by $\mathbf{N}$. $D(\mathbf{r},\mathbf{n})$ is the acquisition dip response (ADR), which gives the illumination response for a plane reflector located at $\mathbf{r}$ with a dipping $\mathbf{n}$. Equation 13 implies that a plane reflector is exclusively illuminated by mirror reflections. Using transform 11, we see that $\mathbf{k}_d=C\mathbf{n}$ is linked to the dipping direction and that $|\mathbf{k}_r|=2k_0\sin i$ is linked to the reflection angle. Considering an isotropic point scatter (i.e., the Born scattering model) $m(\mathbf{r}')\sim\delta(\mathbf{r}')$, we have $M(\mathbf{k})\sim$ const. Substituting $M(\mathbf{k})$ into equation 9 yields

$$D_T(\mathbf{r})=\iint A(\mathbf{r},\mathbf{K}_s,\mathbf{K}_g)d\mathbf{K}_s d\mathbf{K}_g. \quad (14)$$

$D_T(\mathbf{r})$ is the total illumination response, which sums energy from all possible scattering combinations.

The illumination responses for other structures, such as a reflector with a particular curvature or roughness or a layer with random velocity fluctuations, can be obtained using a different $M(\mathbf{k})$. Because of the small size of region V, a simple geometry is usually sufficient for illumination analysis.

NUMERICAL EXAMPLES OF VARIOUS ILLUMINATION MEASUREMENTS

In numerical implementations, the formulations can be discretized. The size of the target region V for the decomposition should be small enough to maintain localized properties of both the wavefield and the model, while large enough to preserve the internal structures of the wavefield and the model (e.g., the wave-propagation direction and the dip of the structure). The local plane-wave decomposition of equation 2 can be conducted on horizontal coordinates by using either local slant stacking or a windowed FFT (Xie and Wu, 2002, Xie et al., 2003). This geometry is consistent with most of the one-way wave-equation-based propagators that choose the vertical direction as the primary propagation direction and apply the transform in the horizontal direction. With these one-way propagators, we can use the depth step as the vertical dimension of V and use the wavelength to determine the horizontal size. The equations developed in this section are in the frequency domain. To calculate illumination responses from multiple frequencies, the response from each individual frequency should be weighted by the source spectrum and summed together. To demonstrate the application of the wave-equation-based illumination analysis, various types of illumination measurements for both 2D and 3D are calculated.

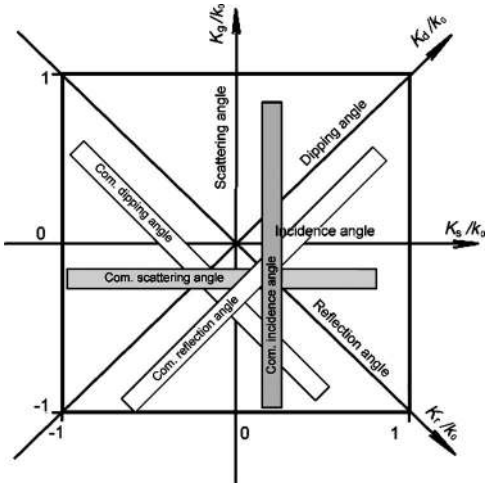

Figure 2. Diagram of the structure of a 2D local illumination matrix. The horizontal and vertical coordinates are K_s and K_g, respectively. The main and auxiliary diagonal directions are horizontal-reflection wavenumber K_r and dipping wavenumber K_d, respectively. Different angle gathers are shown as strips with different orientations.

Local illumination matrix

The illumination matrix can be calculated using equation 10. For a 2D model, the horizontal wavenumber is scalar, and the local illumination matrix $A(\mathbf{r}, K_s, K_g)$ becomes a 2D matrix. Figure 2 is a sketch showing the structure of a 2D local illumination matrix. The horizontal and vertical axes denote the horizontal components K_s and K_g of incidence and scattering wavenumbers, or equivalently, incidence and scattering angles $\theta_s = \sin^{-1}(K_s/k_0)$ and $\theta_g = \sin^{-1}(K_g/k_0)$. The main and auxiliary diagonal directions are horizontal-reflection wavenumber K_r and dipping wavenumber K_d, respectively. As mentioned above, each element (K_s, K_g) in the matrix corresponds to an independent scattering observation of the target. A strip parallel to the vertical direction consists of scatterings with a common incidence angle. Conversely, a strip along the horizontal direction corresponds to scatterings with a common scattering angle. Energy distributed within a strip parallel to the main diagonal is composed of all mirror reflections that contribute to the illumination of a plane-dipping reflector. Similarly, energy distributed within a strip parallel to the auxiliary diagonal corresponds to scatterings that have a common reflection angle. The coordinate transformation 12 rotates the 2D scattering matrix 45°. The energy distribution in the illumination matrix gives the effective acquisition aperture at a local target. To recover the entire target spectrum, properly distributed energy in the illumination matrix is preferred.

As an example, Figure 3 gives local illumination matrices at selected locations in the 2D SEG/EAGE salt model (Aminzadeh et al., 1997). The normalized value $(A/A_{\max})^{1/2}$ is used in the figure, with $A_{\max}$ as the maximum value in the model. The energy occupies the upper-left corner within the matrix resulting from the off-end data acquisition for this model. At a shallow depth, the model is illuminated by wider effective apertures, but the energy spans a relatively narrow aperture at deeper depths. Because of the shadowing effect within the subsalt region, the energy is generally weak and apparently missing for certain dipping and reflection angles. This is the main cause of poor imaging in the subsalt region.

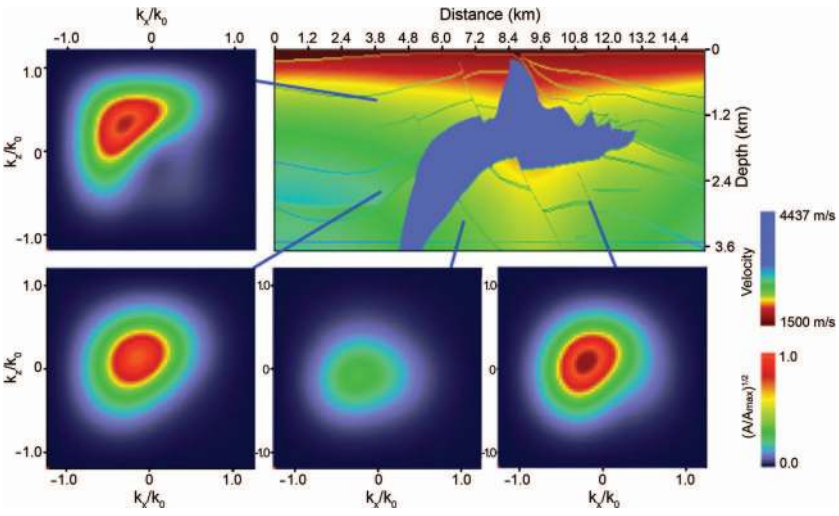

Figure 3. Local illumination matrices at selected locations in the 2D SEG/EAGE salt model. In the sediments at shallow depths, the model is illuminated by wider effective apertures. The illumination spans a relatively narrow aperture at deeper depths, especially in the subsalt region.

Wavenumber-domain illumination

As mentioned above, the illumination matrix can be expressed in the target-wavenumber coordinate $(\mathbf{k}_d, \mathbf{k}_r)$ (see Figures 1 and 2). By integrating $A(\mathbf{r}, \mathbf{k}_d, \mathbf{k}_r)$ over $\mathbf{k}_r$ we project the illumination matrix onto the target-spectrum space,

$$A_d(\mathbf{r}, \mathbf{k}_d) = \int A(\mathbf{r}, \mathbf{k}_d, \mathbf{k}_r) d\mathbf{k}_r, \tag{15}$$

where $A(\mathbf{r}, \mathbf{k}_d, \mathbf{k}_r)$ is obtained from $A(\mathbf{r}, \mathbf{k}_s, \mathbf{k}_g)$ through transformation 12, and the latter can be derived from $A(\mathbf{r}, \mathbf{K}_s, \mathbf{K}_g)$ using

$$A(\mathbf{r}, \mathbf{k}_s, \mathbf{k}_g) = A(\mathbf{r}, \mathbf{K}_s, \mathbf{K}_g)\, \delta(k_{sz} - \sqrt{k_0^2 - K_s^2}) \times \delta(k_{gz} - \sqrt{k_0^2 - K_g^2}), \tag{16}$$

where k_{sz} and k_{gz} are vertical components of $\mathbf{k}_s$ and $\mathbf{k}_g$. In the processes of seismic imaging and diffraction tomography, properly distributed illumination in the target-spectrum space is essential in order to obtain high-resolution results. Several authors (e.g., Wu and Toksöz, 1987; Woodward, 1992) have indicated the importance of wavenumber-domain illumination. For a given acquisition system and velocity model, illumination in the target-spectrum domain can be calculated using equation 15. Similarly, by integrating $A(\mathbf{r}, \mathbf{k}_d, \mathbf{k}_r)$ over $\mathbf{k}_d$, the illumination matrix is projected to the reflection-wavenumber domain,

$$A_r(\mathbf{r}, \mathbf{k}_r) = \int A(\mathbf{r}, \mathbf{k}_d, \mathbf{k}_r) d\mathbf{k}_d, \tag{17}$$

which gives the reflection-angle coverage for all dipping angles at the target location. Figure 4 shows the wavenumber-domain illumination matrices $A_d(\mathbf{r}, \mathbf{k}_d)$ and $A_r(\mathbf{r}, \mathbf{k}_r)$, respectively. Shown in Figure 5 is the illumination matrix $A_d(\mathbf{r}, \mathbf{k}_d)$ at selected locations in the 2D SEG/EAGE salt model. In sediments at the shallow part, good illumination extends to a wide dipping-angle range. The dipping-angle coverage deteriorates with increasing depth, particularly in the subsalt region. In the subsalt region, the acquisition system provides limited vertical resolution and poor horizontal resolution, which explains the poor image quality of steep faults.

Illumination as a function of target-reflection angle

For a target reflector with a local normal vector $\mathbf{n} = \mathbf{n}(\mathbf{r})$, substituting $\mathbf{K}_d = C\mathbf{N}(\mathbf{r})|_{\mathbf{r} \in \text{target}}$ into the illumination matrix $A(\mathbf{r}, \mathbf{K}_d, \mathbf{K}_r)$, we derive the target illumination $A[\mathbf{r}, C\mathbf{N}(\mathbf{r}), \mathbf{K}_r]_{\mathbf{r} \in \text{target}}$ as a function of dipping $\mathbf{n}$ and reflection angle $i = \sin^{-1}(K_r/2k_0)$. Figure 6 shows the reflection-angle distribution of the illumination along four target horizons in a 2D constant-velocity model. We used 181 surface shots to generate the illumination. One of these shots and its 3000-m cable are indicated in Figure 6. The four reflectors (Baina et al., 2002) are labeled from $T1$ to $T4$, in which $T1$ has the largest variation in dipping angles with a maximum value of approximately 40°, $T2$ has a constant dipping angle, $T3$ has a moderate change in dipping angles, and $T4$ is a horizontal reflector. The fan-shaped patterns on these reflectors represent the normalized illumination intensities as a function of reflection angle. Note that the angle coverage decreases with increasing depth. The sections with steep dips have reduced angle coverage and weak intensities. We deliberately choose a constant-background velocity model to show that the illumination is affected by both acquisition aperture and target dipping even in simple scenarios. To obtain correct AVA, compensation of the illumination versus reflection angle is crucial and should be taken into account.

Target-oriented illumination

The ADR $D[\mathbf{r}, \mathbf{n}(\mathbf{r})]|_{\mathbf{r} \in \text{target}}$ on a target can be calculated using equation 13 by substituting the target normal vector $\mathbf{n} = \mathbf{n}(\mathbf{r})|_{\mathbf{r} \in \text{target}}$ into the integration. Figure 7 compares the amplitudes of prestack depth images and computed illuminations on targets for both con-

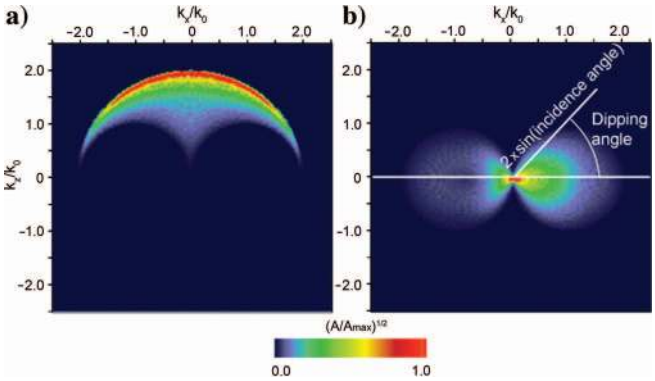

Figure 4. Wavenumber-domain illumination matrices in $\mathbf{k}_d$ domain (a) and $\mathbf{k}_r$ domain (b) for a 2D model.

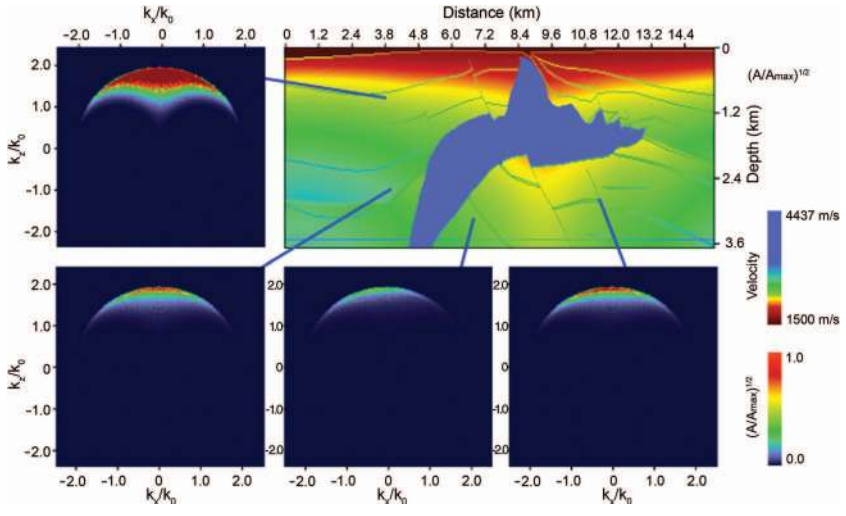

Figure 5. Wavenumber-domain illumination matrices $A_d(\mathbf{r}, \mathbf{k}_d)$ at selected locations in the 2D SEG/EAGE salt model. In the sediments at shallow depths, good illumination extends to a wide dipping-angle range. In the subsalt region, the dipping-angle coverage of the illumination is significantly reduced.

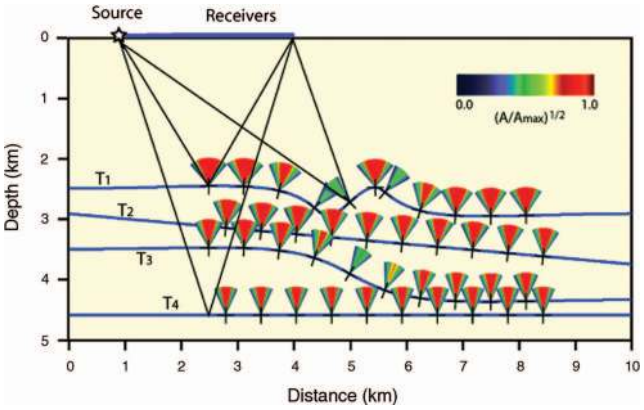

Figure 6. Illumination distribution as a function of reflection angle on the targets. The illumination-angle coverage decreases with the increasing depth. The sections with steep dips have reduced angle coverage and their illumination intensities become weak.

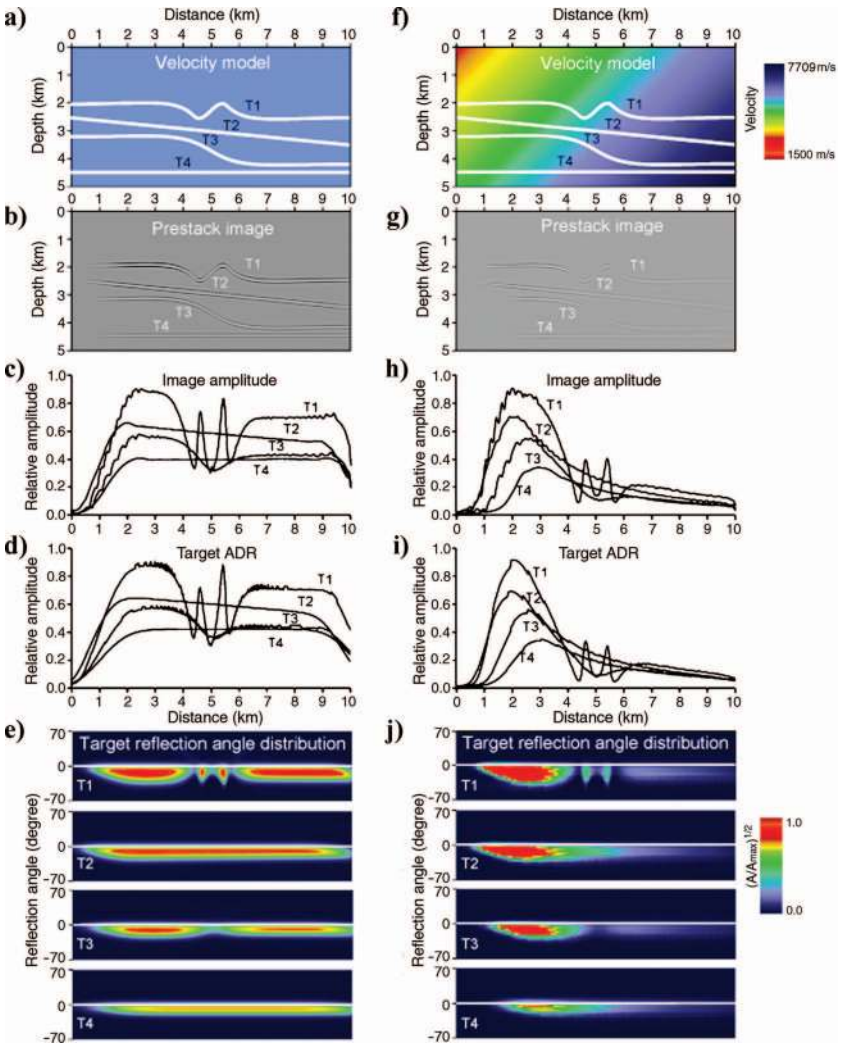

Figure 7. Comparison between the images and illuminations on the targets. The left column is for a constant-velocity model and the right column is for a variable-velocity model. From top to bottom, different rows are (a) velocity model, (b) prestack depth image, (c) amplitudes picked from prestack depth image, (d) ADRs calculated from the illumination analysis, and (e) illuminations as functions of reflection angles. (f) through (j) are similar results for the variable-velocity model. The horizontal coordinates are distance and have been aligned using the same scale.

stant and variable-velocity models. The variable-velocity model and the target reflectors are given by Baina et al. (2002), with all reflectors having a constant reflectivity. The constant-velocity model is created by assigning a velocity of 3.5 km/s throughout the model. In Figure 7, the left column is for the constant-velocity model with (a) the velocity model and target reflectors, (b) prestack depth image, (c) amplitudes picked from the depth image, (d) target ADRs, and (e) the target-illumination coverage as a function of reflection angle. The horizontal coordinates are horizontal distance and have been aligned with the same scale. The results reveal that, even for a constant-velocity model, the image amplitude varies dramatically because of the joint effect of limited acquisition aperture and dipping of the target. The minimum image amplitude corresponds to sections with the steepest dips, where the illumination result shows the narrower reflection-angle coverage. The target ADRs predict the variations of the image amplitudes very well. Such information can be further used as the basis for checking the image quality and correcting the image amplitude. The right column is similar to the left column except that the varying-velocity model is used. In this case, the image amplitude becomes more complex. The illumination analysis, however, still properly predicts the image amplitude.

Volumetric illumination analysis

The volume ADR map, which can be calculated using equation 13, represents the acquisition-dip response as a function of space with the dipping angle as a parameter. Shown in Figure 8 is the 30° ($\mathbf{n} \cdot \hat{\mathbf{e}}_z = \cos 30°$) ADR map for the 3D SEG/EAGE salt model (Aminzadeh et al., 1997). The normalized value $[D(\mathbf{r},\mathbf{n})/D_{\max}]^{1/2}$ is used in the figure, where $D_{\max}$ is the maximum value. In this model, the acquisition system is composed of a source and four cables of 3200-m length. Figure 8a is the ADR in a vertical profile including the source and cables, while Figure 8b shows the ADR in a horizontal slice at a depth of 1000 m. These ADR maps reveal the relationship between the acquisition system, the velocity model, and the illumination. Figure 9a shows an in-line section of the 3D SEG/EAGE salt velocity model. Figure 9c shows the normalized vertical ($\mathbf{n} = \hat{\mathbf{e}}_z$) ADR of the same section. The corresponding-depth image is shown in Figure 9b, which is obtained by a 3D prestack offset-domain wave-equation migration with local reference velocities (Jin et al., 2002). Image shadows are present beneath the salt body, including the missing events on the horizontal baseline. The vertical ADR associated with the illumination of horizontal events shows poor illumination in the same target area. Figure 10 shows a similar relationship between the illumination and the depth image for a horizontal slice at 2500-m depth. Strong total ADR illumination corresponds to the high-quality image at the left side of the model, while a poor image is located in the weak illumination zone.

Summary of different illumination measurements

Table 1 shows various illumination measurements with different levels of detail. Toward the top of the table are high-order illumination matrices, which contain more information, but are composed of larger data sizes. More illumination measurements can be derived from these matrices with additional constraints. Toward the bottom of the table, lower-order measurements consist of more condensed information with compact data sizes. Different levels of measurements can be chosen to meet the specific purposes of the illumination analysis. The measurements with extensive information can be applied to selected locations for comprehensive investigations, while measurements with condensed information can be used to investigate spatial variations of illuminations, such as target-oriented or volumetric analysis.

DISCUSSION

In previous work on illumination analysis (e.g., Wu and Chen, 2002, 2003; Xie and Wu, 2002; Xie et al., 2003), the illumination is formulated for plane reflectors using source and receiver beams with mirror reflections. In this paper, the information regarding the target spatial spectrum is introduced in the formulation. Various illumination measurements can be obtained within this framework. The illumination results can be linked to other analyses, such as diffraction tomography and resolution analysis.

At present, the full-wave method is still too expensive for illumination analysis. The one-way propagator is used instead to calculate the wavefield from sources and receivers to the target. Some approximations are introduced into the one-way propagators. Transmission losses are often neglected. Luo et al. (2004) discussed the difference between illuminations calculated using one-way and full-wave methods and noted that the major factors affecting the illumination are limited acquisition aperture, dipping of the reflector, and accuracy of the propagator. Among these three factors, the first two are usually more crucial than the accuracy of the propagator.

In contrast to seismic imaging, illumination analysis only uses the amplitude of the wavefield. Except for the plane-wave decomposition, the phase information is not used. Therefore, reducing the number of sources and receivers does not cause spatial aliasing and will not seriously affect the illumination calculation. Unlike two-point ray tracing, the wave-equation-based propagator can simultaneously extrapolate waves into a large model space. With a frequency-domain propagator, we can calculate illumination for a number of frequencies or for a single dominant frequency. The result usually provides a satisfactory illumination estimate. The above mentioned approximations can reduce the CPU time considerably and make the wave-equation-based approach an efficient tool for volumetric illumination analysis.

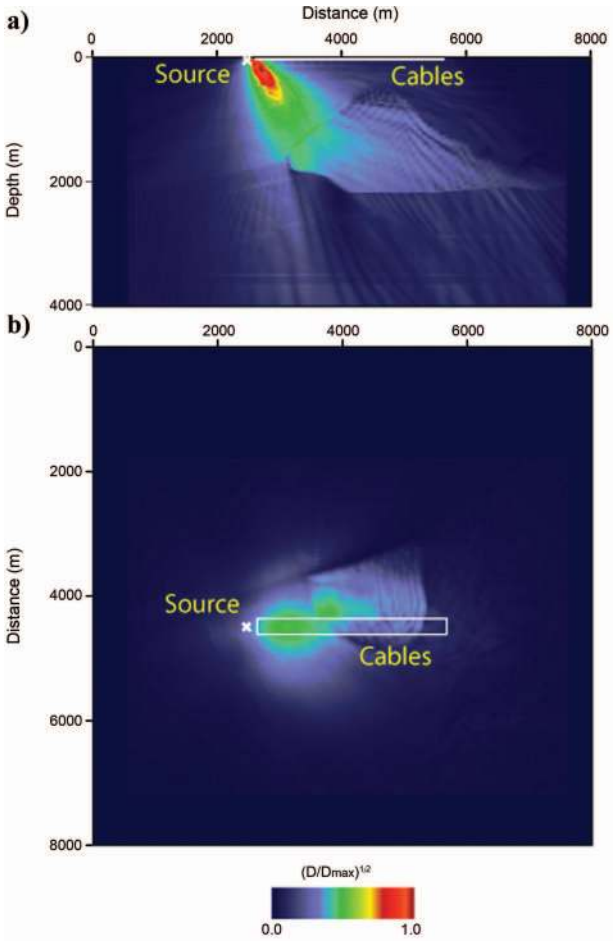

Figure 8. The 30° ADR from a single shot in a 3D model. (a) The illumination of a vertical profile. (b) The illumination of a depth slice at 1000 m. The acquisition system consists of a source and four cables with 3200-m length as indicated in the figure.

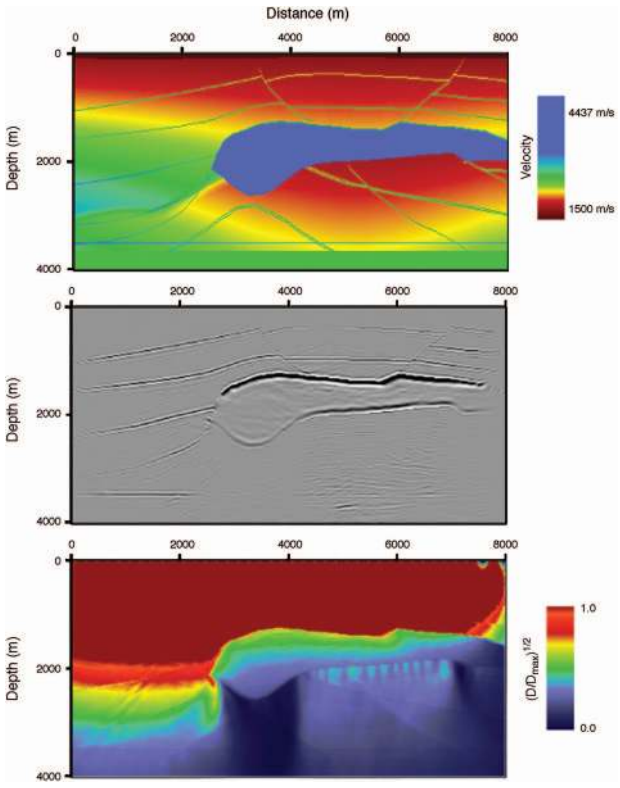

Figure 9. Illumination analysis for an inline section of the 3D SEG/EAGE salt model. (a) The velocity model, (b) the depth image by 3D wave-equation, prestack depth migration, and (c) the corresponding vertical ADR associated with the near-horizontal events. A poor illumination zone is present beneath the salt body. This is consistent with the image shadows where the subsalt structures, including the horizontal baseline, are not well imaged.

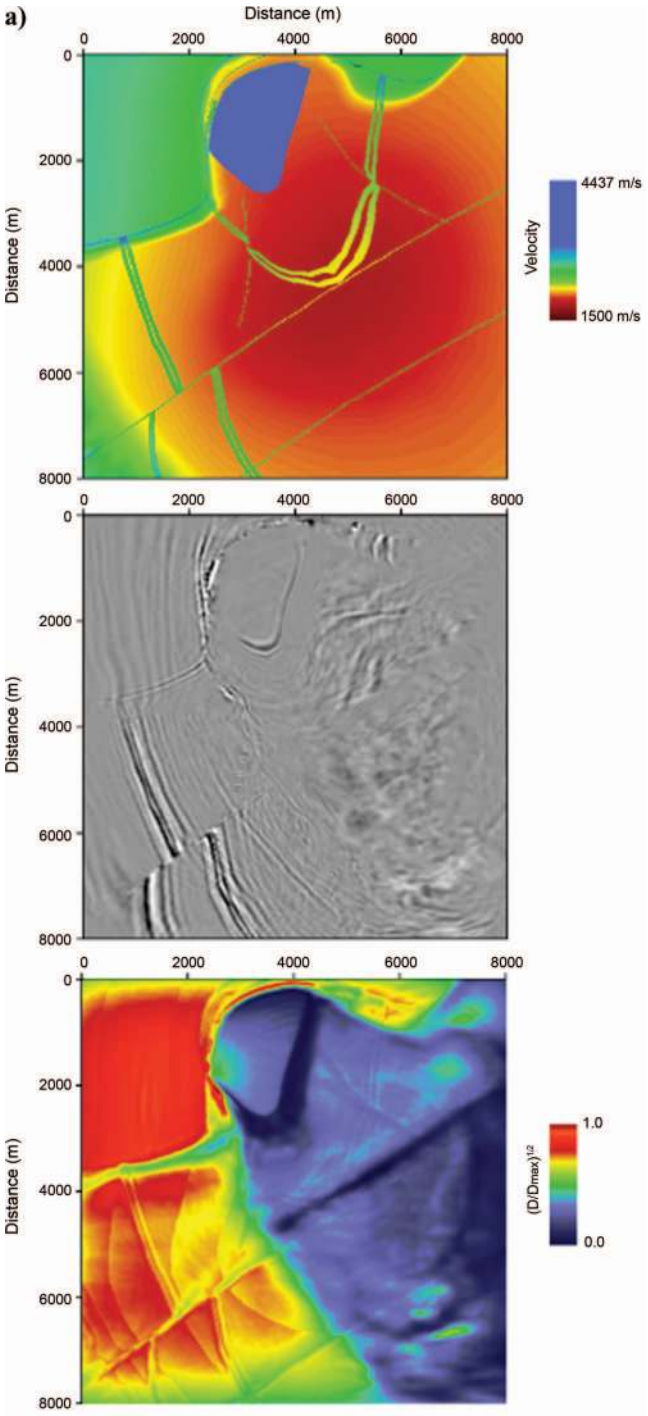

Figure 10. Illumination analysis for a depth slice of the 3D SEG/EAGE salt model. (a) The velocity model at 2500-m depth, (b) a depth image by 3D wave-equation, prestack depth migration, and (c) the total ADR associated with the contributions from all possible dipping events. The depth-image quality is superior at the left portion of the model, which corresponds to the strong illumination, while the image is poor at the right portion, which is related to the weak illumination.

The equations formulated in this paper are based on one source-receiver pair. Complex acquisition geometries (locations of sources, number of streamer cables, receiver locations, navigation directions, etc.) can be composed by summing contributions from multiple source-receiver pairs. Since individual source and receiver wavefields are calculated independently, the wave-equation method is capable of computing illuminations from an irregularly distributed acquisition system.

Table 1. Comparison of different illumination measurements.

	Illumination matrix	$A(\mathbf{r},\mathbf{K}_s,\mathbf{K}_g)$	Toward condensed information and compact data size
	Wavenumber-domain illumination matrices	$A_d(\mathbf{r},\mathbf{k}_d)$ $A_r(\mathbf{r},\mathbf{k}_r)$	
	ADR	$D(\mathbf{r},\mathbf{n})$	
Toward more extensive information and larger data size	Total illumination	$D_T(\mathbf{r})$	
	Target reflection-angle distribution	$A[\mathbf{r};\mathbf{n}(\mathbf{r}),\mathbf{K}_r]_{\mathbf{r}\in\text{target}}$	
	Target ADR	$D[\mathbf{r},\mathbf{n}(\mathbf{r})]_{\mathbf{r}\in\text{target}}$	

CONCLUSIONS

A wave-equation-based method was developed for seismic illumination analysis. Various illumination measurements derived from this method can be used to optimize the acquisition-survey design, evaluate the image quality, and make corrections to the seismic image, resulting in more accurate subsurface physical-parameter retrieval. The current method has the following features.

The wave-equation-based propagator is adopted to calculate the wave propagation. Angle-related information is extracted from the wavefield by local plane-wave analysis. Therefore, this method can properly extrapolate the wavefield in complex media. Velocity smoothing and Fresnel-zone smoothing are no longer required as in the high-frequency, asymptotic, ray-based approach.

The illumination analysis part of the method is independent of its wavefield extrapolation part. Therefore, we conclude that the illumination analysis can be applied to most one-way wave-propagation methods (e.g., the generalized screen propagator and the one-way implicit finite-difference propagator), full-wave-equation methods (e.g., the full-wave, finite-difference scheme), and ray-based or ray-beam-based methods (e.g., the Kirchhoff and Gaussian-beam approaches). This gives us the flexibility to choose different propagators based on the trade-off between their efficiency and accuracy.

Illumination measurements with different levels of detail can be derived from this method. Based on the goal of investigation, we can conduct illumination analysis by choosing the optimal category of measurement. Our wave-equation-based illumination analysis is more efficient than the ray-based method when calculating the volumetric illuminations. Therefore, we conclude that the wave-equation-based illumination analysis provides a flexible and efficient tool to calculate target-oriented or volumetric illuminations in 2D and 3D complex models.

ACKNOWLEDGMENT

This research is supported by the DOE/BES project at the University of California, Santa Cruz, under Grant DE-FG02-04ER15530. Facility support from the W. M. Keck Foundation is also acknowledged. Contribution 483 of the CSIDE, IGPP, University of California, Santa Cruz.

REFERENCES

Aminzadeh, F., J. Brac, and T. Kunz, 1997, SEG/EAGE 3-D modeling series, no. 1, 3-D salt and overthrust models: SEG.

Baina, R., P. Thierry, and H. Calandra, 2002, 3D preserved-amplitude prestack depth migration and amplitude versus angle relevance: The Leading Edge, **21**, 1237–1241.

Bear, G., C. Liu, R. Lu, and D. Willen, 2000, The construction of subsurface illumination and amplitude maps via ray tracing: The Leading Edge, **19**, 726–728.

Berkhout, A. J., L. Ongkiehongz, A. W. F. Volker, and G. Blacquière, 2001, Comprehensive assessment of seismic acquisition geometries by focal beams — Part I: Theoretical considerations: Geophysics, **66**, 911–917.

Biondi, B., 2002, Stable wide-angle Fourier finite-difference downward extrapolation of 3-D wavefields: Geophysics, **67**, 872–882.

Gelius, L. J., I. Lecomte, and H. Tabti, 2002, Analysis of the resolution function in seismic prestack depth imaging: Geophysical Prospecting, **50**, 505–515.

Hoffmann, J., 2001, Illumination, resolution, and image quality of PP- and PS-waves for survey planning: The Leading Edge, **20**, 1008–1014.

Huang, L. J., M. Fehler, and R. S. Wu, 1999, Generalized local Born Fourier migration for complex structures: Geophysics, **64**, 1524–1534.

Jin, S., C. C. Mosher, and R. S. Wu, 2002, Offset-domain pseudoscreen prestack depth migration: Geophysics, **67**, 1895–1902.

Jin, S., and D. Walraven, 2003, Wave equation GSP prestack depth migration and illumination: The Leading Edge, **22**, 606–610.

Jin, S., R. S. Wu, and C. Peng, 1998, Prestack depth migration using a hybrid pseudo-screen propagator: 68th Annual International Meeting, SEG, Expanded Abstracts, 1819–1822.

Lecomte, I., H. Gjøystdal, and Å. Drottning, 2003, Simulated prestack local imaging: a robust and efficient interpretation tool to control illumination, resolution, and time-lapse properties of reservoirs: 73rd Annual International Meeting, SEG, Expanded Abstracts, 1525–1528.

Luo, M., J. Cao, X. B. Xie, and R. S. Wu, 2004, Comparison of illumination analysis using one-way and full-wave propagators: 74th Annual International Meeting, SEG, Expanded Abstracts, 67–70.

Mosher, C. C., S. Jin, and D. J. Foster, 2001, Migration velocity analysis using common angle image gathers: 71st Annual International Meeting, SEG, Expanded Abstracts, 889–892.

Muerdter, D., M. Kelly, and D. Ratcliff, 2001, Understanding subsalt illumination through ray-trace modeling, Part 2: Dipping salt bodies, salt peaks, and nonreciprocity of subsalt amplitude response: The Leading Edge, **20**, 688–697.

Muerdter, D., and D. Ratcliff, 2001a, Understanding subsalt illumination through ray-trace modeling, Part 1: Simple 2-D salt models: The Leading Edge, **20**, 578–594.

———, 2001b, Understanding subsalt illumination through ray-trace modeling, Part 3: Salt ridges and furrows, and the impact of acquisition orientation: The Leading Edge, **20**, 803–816.

Prucha, M. L., B. L. Biondi, and W. W. Symes, 1999, Angle-domain common image gathers by wave-equation migration: 69th Annual International Meeting, SEG, Expanded Abstracts, 824–827.

Rickett, J. E., 2003, Illumination-based normalization for wave-equation depth migration: Geophysics, **68**, 1371–1379.

Ristow, D., and T. Ruhl, 1994, Fourier finite-difference migration: Geophysics, **59**, 1882–1893.

Schneider, W. A., and G. A. Winbow, 1999, Efficient and accurate modeling of 3-D seismic illumination: 69th Annual International Meeting, SEG, Expanded Abstracts, 633–636.

Schuster, G. T., and J. Hu, 2000, Green's function for migration: Continuous recording geometry: Geophysics, **65**, 167–175.

Stoffa, P. L., J. T. Fokkema, R. M. D. Freire, and W. P. Kessinger, 1990, Split-step Fourier migration: Geophysics, **55**, 410–421.

Volker, A. W. F., G. Blacquière, A. J. Berkhout, and L. Ongkiehong, 2001, Comprehensive assessment of seismic acquisition geometries by focal beams — Part II: Practical aspects and examples: Geophysics, **66**, 918–931.

Woodward, M. J., 1992, Wave-equation tomography: Geophysics, **57**, 15–26.

Wu, R. S., and L. Chen, 2001, Beamlet migration using Gabor-Daubechies frame propagator: 63rd Annual Conference and Exhibition, EAGE, Extended Abstracts, P074.

———, 2002, Mapping directional illumination and acquisition-aperture efficacy by beamlet propagators: 72nd Annual International Meeting, SEG, Expanded Abstracts, 1352–1355.

———, 2003, Prestack depth migration in angle-domain using beamlet decomposition: Local image matrix and local AVA: 73rd Annual International Meeting, SEG, Expanded Abstracts, 973–976.

Wu, R. S., L. Chen, and X. B. Xie, 2003, Directional illumination and acquisition dip-response, 65th Annual Conference and Exhibition, EAGE, Extended Abstracts, P147.

Wu, R. S., and M. N. Toksöz, 1987, Diffraction tomography and multisource holography applied to seismic imaging: Geophysics, **52**, 11–25.

Xie, X. B., S. Jin, and R. S. Wu, 2003, Three-dimensional illumination analysis using wave-equation based propagator: 73rd Annual International Meeting, SEG, Expanded Abstracts, 989–992.

Xie, X. B., C. C. Mosher, and R. S. Wu, 2000, The application of wide-angle screen propagator to 2D and 3D depth migrations: 70th Annual International Meeting, SEG, Expanded Abstracts, 878–881.

Xie, X. B., and R. S. Wu, 1998, Improve the wide-angle accuracy of screen method under large contrast: 68th Annual International Meeting, SEG, Expanded Abstracts, 1247–1250.

———, 2002, Extracting angle domain information from migrated wavefield: 72nd Annual International Meeting, SEG, Expanded Abstracts, 1360–1363.

———, 2005, Multicomponent prestack depth migration using elastic screen method: Geophysics, **70**, S30–S37.